Combating Li Metal Deposits in All-Solid-State Battery via the Piezoelectric and Ferroelectric Effects

Jianming Tao[1,2,3], Yue Chen[5], Aman Bhardwaj[2], Lang Wen[1,3], Jiaxin Li[1,3,4], Oleg V. Kolosov[5], Yingbin Lin[1,3,4,*], Zhensheng Hong[1,2,*], Zhigao Huang[1,3,4], Sanjay Mathur[2,*]

[1]College of Physics and Energy, Fujian Normal University, Fujian Provincial Solar Energy Conversion and Energy Storage Engineering Technology Research Center, Fuzhou, 350117, China.

[2]Institute of Inorganic Chemistry, University of Cologne, Greinstr.6, 50939 Cologne, Germany.

[3]Fujian Provincial Key Laboratory of Quantum Manipulation and New Energy Materials, Fuzhou, 350117, China.

[4]Fujian Provincial Collaborative Innovation Center for Advanced High-Field Superconducting Materials and Engineering, Fuzhou, 350117, China.

[5]Physics Department, Lancaster University, Lancaster LA1 4YB, United Kingdom.

[*]Corresponding author(s): Yingbin Lin, Zhensheng Hong, Sanjay Mathur.

Tel: +86-591-2286-8132

Fax: +86-591-2286-8132

E-mail: yblin@fjnu.edu.cn; zshong@fjnu.edu.cn; sanjay.mathur@uni-koeln.de

Abstract

All-solid-state Li-metal batteries (ASSLBs) are highly desirable due to their inherent safety and high energy density, however, the irregular and uncontrolled growth of lithium filaments is detrimental to interfacial stability and safe operation that points out the dire need of new electrode materials with high ionic conductivity and electrochemical compatibility with Li ions. Herein, we report on the incorporation of piezo/ferroelectric $BaTiO_3$ (BTO) nanofibers into solid electrolytes and determination of electric field distribution due to BTO inclusion that effectively regulates the nucleation and growth of Li-dendrites. Theoretical simulations predict that the piezoelectric effect of BTO embedded in solid-electrolyte reduces the driving force of dendrite growth at high curvatures, while its ferroelectricity reduces the overpotential, which helps to regularize Li deposition and Li^+ flux. Polarization reversal of soft solid electrolyte was identified for the first time via the improved piezo force microscopy that further confirmed a regular deposition and morphology alteration of Li. As expected, the ASSLBs operating with $LiFePO_4$/Li and PEO/Garnet solid electrolyte containing 10% BTO additive showed a steady and long cycle life with a reversible capacity of 103.2 mAh g^{-1} over 500 cycles at 1 C. Moreover, the scalable pouch cells prepared with piezo-enhanced materials demonstrated comparable cyclability and flexibility indicating new opportunities for Li-metal anodes in ASSLBs. Furthermore, this strategy is also validated towards sulfide electrolytes, which is promising to improve the critical current density and cycling performance, demonstrating its universal and promising application for integration of Li metal anodes in solid-state batteries.

Keywords: *solid-state battery; lithium dendrite; piezo-ferroelectric effect; solid electrolyte.*

1. Introduction

In the quest of most promising "beyond Li-ion batteries" configuration , all-solid-state Li batteries (ASSLBs) have been extensively investigated to meet the growing demand for mobile energy providers and large-scale energy storage systems, mainly due to their high energy density, excellent safety characteristics, and superior cycle stability.[1-3] Unfortunately, the notorious dendrite growth caused by uncontrolled electrodissolution of Li metal results in concomitant huge volume change, and formation of massive dead Li dendrite that hampers long-cycling life and high safety desired in ASSLBs.[4,5] In comparison to the liquid electrolytes, solid electrolytes with lower deformability and higher interfacial resistance usually tends to have a poor critical current density, resulting in nucleation and growth anisotropic Li filaments.[6-8] Even when using the sulfide-based electrolyte and a Li-In alloy, Luo *et al.*[9] reported that the 'Li-In dendrites' are also found at high current densities.

Based on the classical electrochemical theory, the formation and evolution of Li dendrites is essentially a result of the dynamic competition between electrodissolution of Li metal and electrodeposition of Li$^+$ ions with concomitant reduction.[10,11] Specifically, the spatial distribution of these factors determines the probability of dendrite formation, and the evolution of their growth rate in relation to the operation time. Therefore, improving the ionic conductivity of the solid electrolyte,[12] enhancing and equalizing the electronic conductivity in electrode,[13] and ensuring their seamless interfacial contact with a low resistance[14-16] are the typical strategies to control lithium dissolution kinetics at solid electrolyte interfaces that consequently reduces the Li dendrite formation in ASSLBs. However, the coexistence of these material characteristics in a single solid electrolyte is rare and painstaking to obtain a suitable combination even using machine learning algorithms,[17,18] which severely limits the development of high-performance ASSLBs.

Although the above-mentioned factors are deterministic for the non-equilibrium

dynamics of Li deposition, the driving force which represents the kinetic coefficient of electrochemical reaction for dendrite growth usually depends on the activation overpotential.[11,19-21] The larger activation overpotential generally promotes the irregular electrodissolution and accelerate the dendrite formation in the early stage. Kim *et al.*[22] reported that lithiated ZnO nanorods enable interfacial integrity, reduce the overpotential to enable dendrite-free cycling at high current density. The use of additional electric field between functional electrolyte and anode was proposed to directly reduce overpotential and has proved to be an effective measure in controlling and circumventing Li deposition. For example, Liu *et al.*[23] designed a PVDF-based solid electrolyte whose piezoelectrically generated electric field created by the extrusion during Li-plating can reduce the local overpotential and promote uniform Li-deposition. Wang *et al.*[24] used the polarization field between BaTiO$_3$ porous scaffold and electrolyte to suppress the electrical field gradients that improved the morphological control over Li deposition. However, these strategies depend on the functional characteristics of solid electrolytes limiting them to few specific material compositions and making their universal implementation rather challenging. Moreover, the specific mechanism and influence of generated additional electric fields on Li deposition remains unclear.

Motivated by the above concerns and inspired by the recent findings on multi-modal electrode materials, we incorporated piezoelectric BaTiO$_3$ (BTO) nanofibers into the most widely used PEO-based solid electrolyte, and demonstrated the successful reversal of their polarization and, hence, modification of localized ferroelectric effect in the electrolyte using piezo force microscopy. Moreover, the theoretical simulation reported here suggested that the piezoelectricity linked electrical field in solid electrolytes would reduce the driving force of dendrite growth at high curvatures, and the ferroelectricity linked electrical field reduces the overpotential, thus regularizing Li deposition process and the distribution of Li$^+$ flux. As

expected, the morphology of Li deposits became more ordered and uniform with increasing piezo/ferroelectric field. In addition, the corresponding LiFePO$_4$/Li button and pouch batteries operating with BTO-reinforced electrode materials were found to exhibit better electrochemical performance. Furthermore, this simple strategy is also proven to help improve the critical current density and cycling performance of the Li$_6$PS$_5$Cl electrolyte. Finally, this work offers new insights into universal electrolyte design concepts based on multi-functional composite electrode materials that are beneficial for high-energy-density ASSLBs.

2. Results and discussion

The phase-field model was carried out to describe the evolution of morphologies of lithium deposits under weak solid-state interactions and dispersion forces, presence of either piezoelectric or ferroelectric field, and coexistence of both piezo- and ferroelectric fields, respectively. The specific simulation formulae and calculation models are described in detail in the Supporting Information (SI). As depicted in **Figure 1**a, the driving force (representing the relative growth rate of Li dendrites) manifested in the bulging area is larger than that at the planar interface region due to the local increase of the polarization, thus leading to the rapid formation and growth of dendrites. We also noticed that the activation overpotential also exerts significant influence on the evolution and magnitude of the driving force suggesting that the smaller the activation overpotential, the lower the driving force. Interestingly, based on the computational data, extra piezo/ferroelectric fields were found to be helpful in reducing the activation overpotential thus guiding the growth of planar (isotropic) Li deposits.

Figures 1b-d present the 2D snapshots of the Li-atom concentration, Li$^+$ concentration, and driving force after an evolution time of 86 s. In contrast to other two scenario, the Li

morphologies in the weak solid-state interaction evolved from an initial tiny protrusion (see SI, Figure S1) to several large and long dendrites rapidly. It is noteworthy that the roots of these dendrites are relatively thin and thus prone to fracture to form dead amount of Li that no longer contributes to electrochemical cycling, thus decreasing the overall cell capacity and performance efficiency. In addition, the Li^+ concentration for weak-field scenario (Figure 1c) also exhibited an uneven distribution, especially producing a huge concentration gradient at the dendrite tip with a maximum value about 6 above the bulk Li^+ concentration. Local Li^+ concentration intensifies high concentration polarization and causes the aggregation of the driving force for dendrite formation.[19, 25] Under the influence of such strong concentration gradient and low ionic conductivity of the solid electrolyte, the Li deposition represents a non-compact irregular morphology (shown in the color distribution of Figure 1b), which would lead to unpredictable electrode characteristics ultimately leading to a catastrophic battery failure.

The simulation of Li dendrite deposition under the additional electric field generated due to piezoelectric properties of the pre-stressed BTO nanofibers revealed that the larger piezoelectric field responds to an electrical filed to the high curvature, which could alleviate the growth and spread of dendrites. However, there are still semi-circular Li formation evident, indicating that this electrical filed not sufficient to reverse the initial electrodissolution processes observed as protrusion. As shown in SI, Figure. S2, the piezoelectric field reduces the overpotential gradient at the tip, which in turn reduces the Li^+ concentration, thus obtaining a smaller local Li^+ concentration and driving force. In relative terms, the ferroelectric effect is more efficient and resulted in a nearly flat Li deposit. But unfortunately, its Li^+ concentration distribution presented a wide transition layer and a maximum concentration of up to 1.9 times, which causes polarization in larger areas and potentially degrades solid electrolytes, thus not ideal for long-term deposition.[26] The

combination of both piezo- and ferroelectric fields delivered the most uniform Li deposition, Li^+ flux transfer, driving force, and overpotential evaluation during the initial 80 s. Even after the evolution of up to 200 s, the evaluation videos in SI, S1-4 manifested that it remains a stable planar deposition state with regular interface, when compared to other two cases suggesting the superior influence of polarization effects caused by BTO dispersoids. Our hypothesis is that a reverse deflection of the piezoelectricity linked electrical field and the maintenance of the ferroelectricity linked electrical field during the Li deposition process, could accelerate the removal of Li dendrites and ensure a smooth interface necessary for long-term stability.
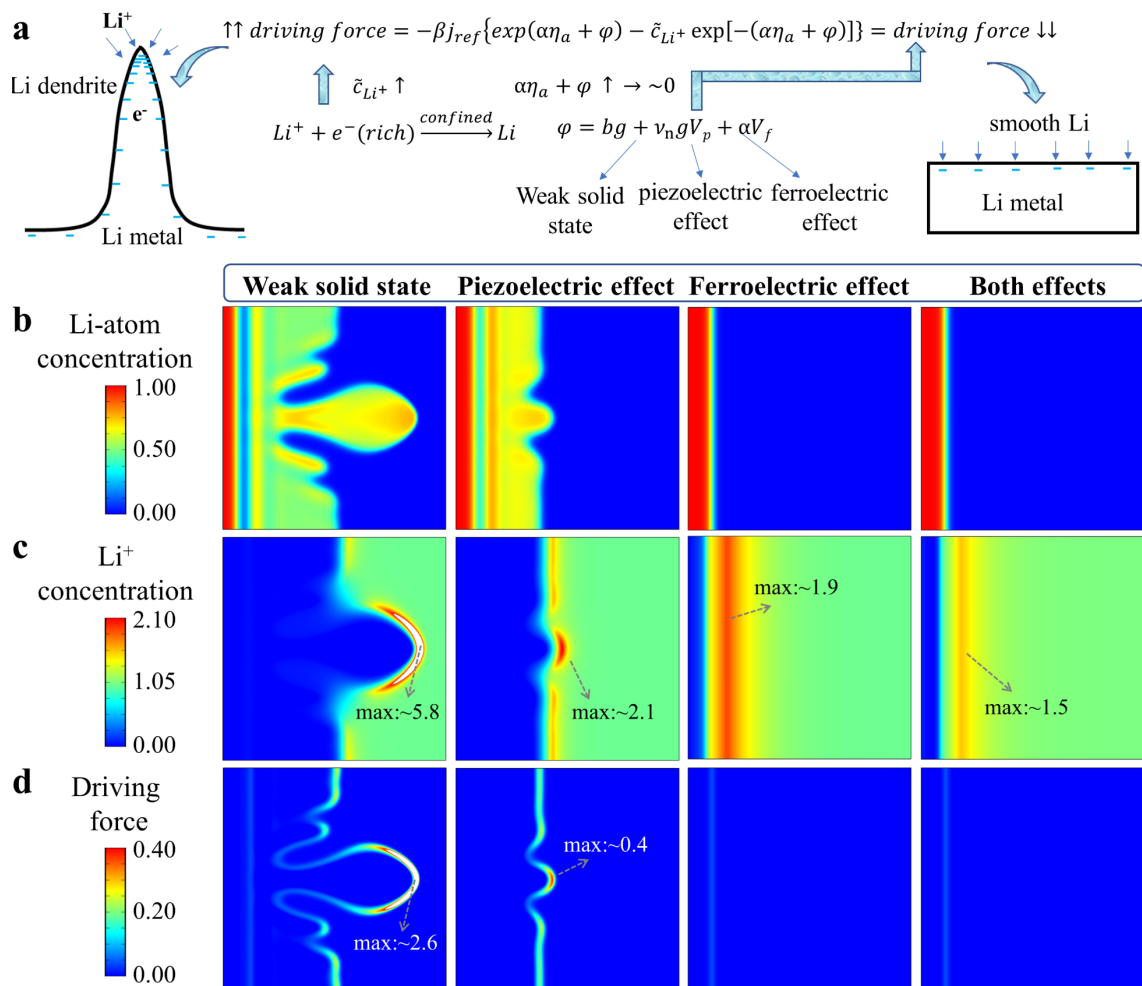

Figure 1. (a) Schematic diagram of Li deposition in ASSLBs. See SI for the details of the equation derivations. (b) the Li-atom dimensionless concentration distribution, (c) the Li^+ concentration distribution, and (d) the driving force after 86 s of 1 mA cm^{-2} for the battery with weak solid-state, piezoelectric effect, ferroelectric effect, and both piezo/ferroelectric effects, respectively.

Solid electrolytes exhibiting both high Li$^+$ conductivity and piezo/ferroelectric properties are rare and only reported in a few classes, such as Li$_3$ClO,[27] Li$_2$O-LiNbO$_3$-B$_2$O$_3$ glass [28], however their intrinsic shortcomings, such as narrow electrochemical windows and high reactivity toward Li metal marginalize their application potential in devices. Therefore, we selected a typical ferroelectric material, BaTiO$_3$, as an additive to the common electrolytes to verify those positive effects under real-life conditions. As illustrated in **Figure 2**a, BaTiO$_3$ (BTO) nanofibers were prepared by electrostatic spinning, and then simply mixed with Li$_{6.7}$La$_3$Zr$_2$Al$_{0.1}$O$_{12}$ (LLZAO), PEO, LiTFSI to obtain the PEO-based composite electrolyte in which the weight ratios of BTO was varied from 0% to 10%. The as-prepared BaTiO$_3$ powder exhibited a typical tetragonal phase by the XRD pattern (SI, Figure S3a) and demonstrated fiber-like morphologies with average radial dimensions ranging between 200-300 nm (Figure 2b and SI, Figures S3b-c). The ionic conductor additive, LLZAO (Figure S4), possessed an irregular particle with an average grain size greater than 3 μm. The XRD pattern (see SI, Figure S4a) revealed a cubic phase with however a little amount of Li$_4$ZrO$_4$ present as a secondary phase.[29] As displayed in Figure 2c-d and Figure S5 (SI), the linear morphology of additive is increasingly visible inside the solid electrolyte with increasing BTO content. Furthermore, the EDS elemental mapping images of samples containing 10%BTO (Figure 2e) indicated that BTO was uniformly distributed in PEO-based solid electrolyte. Although the volumetric content of BTO is just half in comparison to that of LLZAO, its contact area with PEO was much larger due to the smaller particle size. The XRD pattern (Figure 2f) confirmed that mixing with PEO does not change the crystalline structure and phase of BTO thus indicating that no unwanted interfacial reactions occurred during the fabrication of the composite electrode.
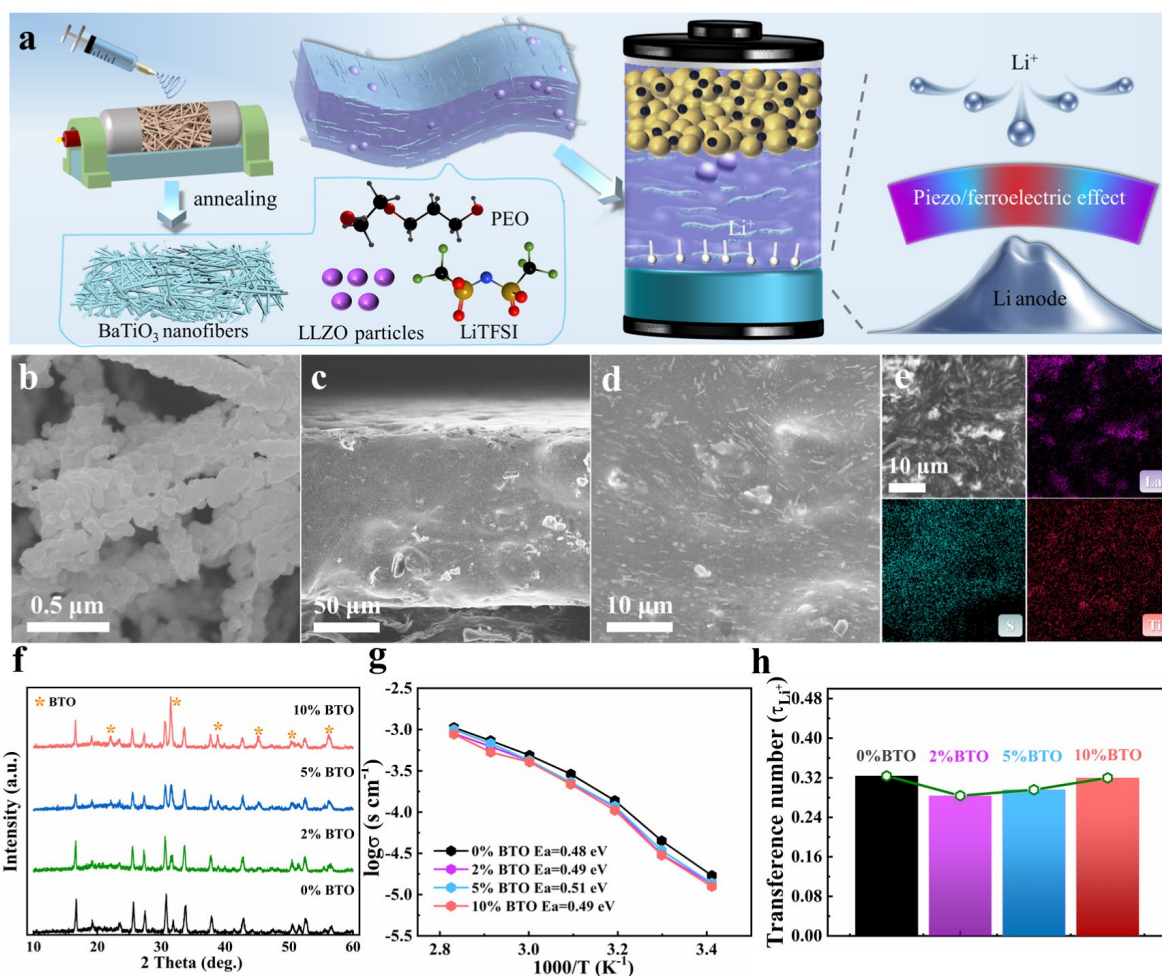
Figure 2. (a) Schematic diagram of composite solid electrolyte containing BaTiO$_3$ nanofibers with ferroelectric effect. (b) SEM image of BaTiO$_3$ nanofibers. (c) Cross-sectional SEM image of 10%BTO. (d) The EDS elemental mapping images of La, S, and Ti for 10%BTO. (f) XRD patterns of all typical electrolytes. (g) Arrhenius plots of all typical electrolytes for the calculation of the activation energy. (h) Li$^+$ transfer number chart of all typical electrolytes.

To evaluate the ionic conductivity of these electrolytes, SS (stainless steel)/solid electrolyte/SS cells were assembled and tested at different temperatures (SI, Figure S6-7). As displayed in Figure 2g, the ionic conductivity and activation energy of 10% BTO at 60 °C were found to be 3.5×10^{-4} S cm^{-1} and 0.49 eV, which is slightly inferior than the other samples. Besides, the polarization curves (SI, Figure S8) and the calculated Li$^+$ transfer number (Figure 2h) further indicate, a minor negative effect of BTO on Li$^+$ transfer. In addition, the linear sweep voltammetry (SI, Figure S9) measurements confirm that all types of the electrolytes have a similar electrochemical window and a high oxidative potential of

~4.6 V, which allowed to compare the piezo/ferroelectric field effects under comparable conditions.

The piezo/ferroelectric properties of the single BTO nanofiber are studied by the piezo force microscopy (PFM, **Figure 3**a, the detailed information is shown in SI, Figure S10). It can be seen in Figure 3b that the BTO nanofiber exhibits significant mechanical displacement with the change of applied bias. Many internal piezoelectric domains were also found in the PFM phase contrast exhibiting ferroelectric properties of the samples.[30,31] At the applied DC bias of -4 V, the domain orientation showed a clear reversal. The polarization reversal was observed when applying a reverse bias of +4 V. Figure 3c presents the PFM phase hysteresis loops and characteristic amplitude " butterfly curves " on the BTO surface. The phase greater than 90° in the phase transition region indicates the BTO to be a ferroelectric component.[32-34] Additionally, the wide voltage range of up to 1.3 V toward phase hysteresis is sufficient for most interfaces with overpotential below 0.5 V to limit the polarization field.[35]

Figure 3d shows the CV curves of SS/solid electrolyte/SS cells at 60 °C. According to the plate capacitor formula, [36] the relative permittivity was calculated and summarized in Table S2 (SI). With increasing BTO content, the relative permittivity was also found to increase and the addition of 10% BTO demonstrated the highest value, which is 4 times higher than samples without piezo-additive (0% BTO). It was evident that the ferroelectric BTO additive does greatly improve the dielectric properties of solid electrolytes which is an important parameter for depolarization field and local Li^+ transport. [35,37] Besides, we combined for the first time the peak force tapping imaging mode [38] with off-resonance PFM, that we call PF-PFM, which allows detecting the piezo/ferroelectric signals of solid electrolytes with soft and viscous components. The detailed measure was discussed and shown in the SI, and the results allowed to verify reliability of such an approach as presented

in SI, Figure S11. The PF-PFM amplitude at a bias of -2 V for all solid electrolytes (Figure 3e) revealed that the infiltration of BTO does let the electrolyte have a strong feedback electrical signal. Compared with the near back-bottom result of sample with 0% BTO, samples with 10% BTO exhibited a clear and maximum electrical signal. The phase at a bias of -0.5 V for 10% BTO addition further confirmed that BTO can respond to the applied electric field and produce phase reversal even when buried in the solid electrolyte.

Furthermore, recent reports have pointed out that the electrical double layer could bring a local reversal of the surrounding ferroelectric electrolyte in the batteries with metal as an electrode and ferroelectric as the electrolyte, and thus bring a fixed depolarization field without being triggered by the applied electric field.[39,40] In this case, the Li^+ transport and deposits in the solid electrolyte are affected by interface overpotential and extra piezo/ferroelectric field. To distinguish the effect of additional piezo/ferroelectric field on Li deposition, the Li/Solid electrolyte (SE)/Li cells were assembled and one-side Li deposition was performed by a single discharge step at a current density of 0.5 mA cm^{-2}. Meanwhile, in-situ EIS test was performed every 10 min during the deposition (discharge process). With increasing BTO content, the polarization potential becomes smaller and the time before the potential drops to ~0 elongates (Figure 3g) due to the piezo/ferroelectric depolarization field and regularized Li deposit morphologies. Figure S12 (see SI) and Figure 3h further presents the surface morphology of deposited Li metal as a function of incorporated BTO content. 0% BTO shows uneven deposition and small flakes began to emerge just after 3.4 h (at ~1.5 mAh cm^{-2}). In contrast, the deposition with 2% BTO is relieved and become more uniform, with some inhomogeneous pores and small tip particles. With the increasing BTO content, the Li deposition tends to be homogenized and the critical deposition capacity increases. Undoubtedly, 10% BTO shows the longest deposition time of 12 h with a lowest overpotential of 0.267 V, and smoothest regular deposited Li surface. This is consistent with

the simulation results that the enhanced piezo/ferroelectric properties correspond to the improved ordered deposition, suggesting their positive effect.
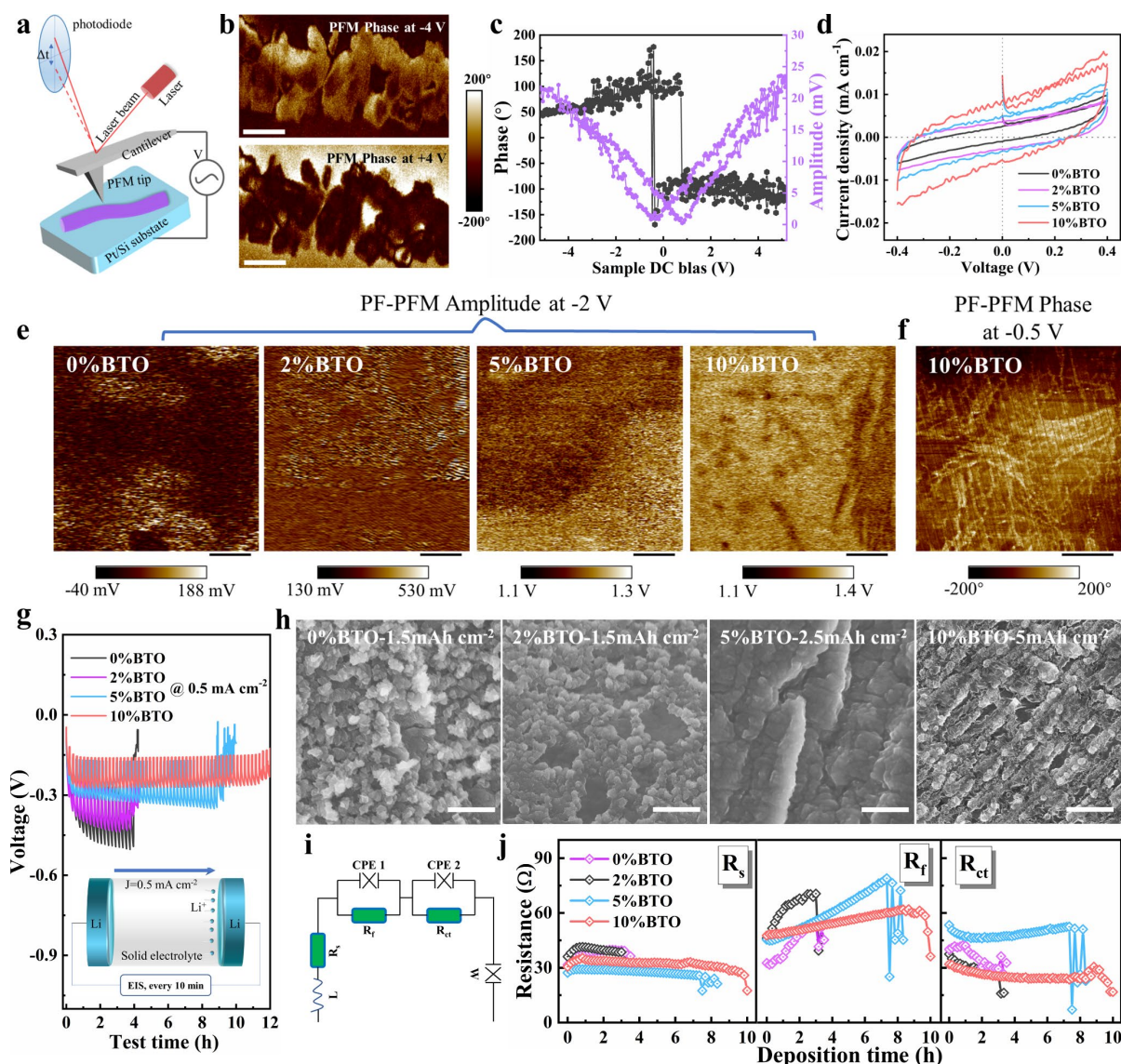

Figure 3. (a) Schematic representation of the PFM measurement for the BaTiO$_3$ single nanofiber. (b) the PFM phase of the BTO single nanofiber at -4V and +4V bias voltage, and the spatial scale bar is 100 nm. (c) the amplitude/phase-voltage loop for the BaTiO$_3$ single nanofiber. (d) Cyclic voltammetry curves of SS/solid electrolyte/SS cells at 60 °C between -0.4 V and 0.4 V. (e) the PF-PFM amplitude images for all solid electrolyte samples at a bias of -2 V. (f) the PF-PFM phase image for 10%BTO at a bias of -0.5 V. The spatial scale bar is 2 μm for all PF-PFM image. (g) The voltage-time curves of the Li/solid electrolytes/Li cell at 0.5 mA cm^{-2}. (h) the surface morphologies of deposited Li anode obtained from Li/solid electrolytes/Li cell after different times of 0.5 mA cm^{-2}. The spatial scale bar is 1 μm for all surface images. (i) the equivalent circuit and (j) The fitted results including R$_s$, R$_f$, and R$_{ct}$ for the Li/solid electrolytes/Li cell at each testing.

To further evaluate the change of resistance during Li deposition, the Nyquist plots from the in-situ EIS results were collected and shown in Figure S13 (SI). Fitted with the equivalent circuit (Figure 3i), the isolated resistance, such as the electrolyte resistance (R_s), the resistance of SEI film (R_f), and the charge transfer resistance (R_{ct}) were all calculated in Figure 3j. In contrast to the similar results of R_s and R_{ct} for all samples, R_f exhibits different increase trends with deposition time. The increase of R_f indicates the increase of SEI film quantity or the deterioration of composition on the deposited Li surface.[41,42] With increasing BTO content, the increasing trend of R_f gradually decreases. The sample with 10% BTO showed the minimum slope, confirming the stable deposition behavior under the extra piezo/ferroelectric field.
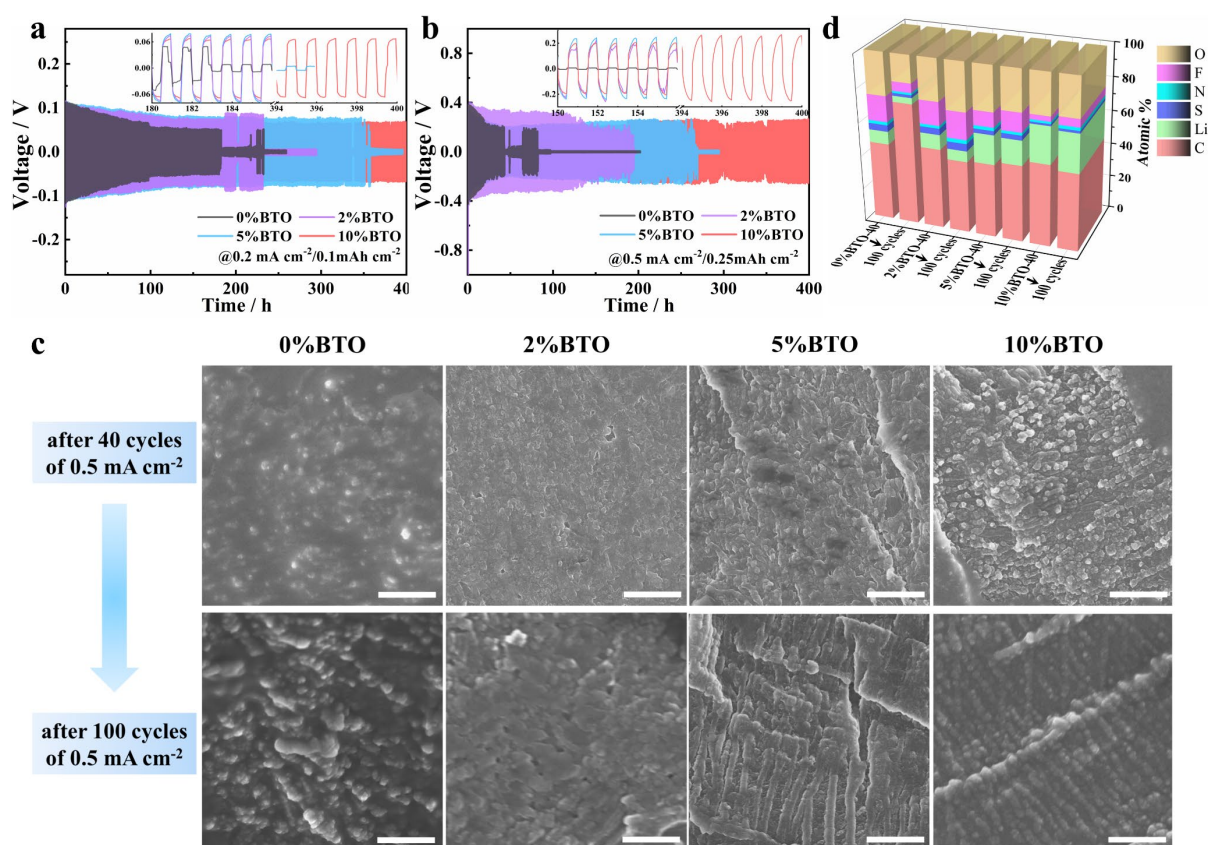

Figure 4. Cycling performance of Li/solid electrolytes/Li batteries by using all typical electrolytes with a current density of a) 0.2 mA cm^{-2}/0.1 mAh cm^{-2} and b) 0.5 mA cm^{-2}/0.25 mAh cm^{-2}, the inset show the enlarged voltage profiles at typical periods. (c) the surface morphologies of the Li anode obtained from Li/solid electrolytes/Li cells after different cycles of 0.5 mA cm^{-2}. The spatial scale bar is 2 μm for all surface images. (d) the relative content of elements in Li anode surface after 40 and 100 charge/discharge

cycles.

The reversibility and stability of Li deposition are important metrics for reliable ASSLBs. The Li plating/stripping curves at 0.2 mA cm^{-2}/0.1 mAh cm^{-2} and 0.5 mA cm^{-2}/0.25 mAh cm^{-2} were examined by galvanostatic discharge/charge voltage profiles in symmetric Li/SE/Li cells, as presented in Figures 4a and b, respectively. Consistent with the results obtained in one side deposition, the cell's overpotential is reduced and the homologous cycling performance is also improved as the BTO content was increased. Functionally enhanced by the depolarization field and regularized Li deposition due to the enhanced piezo/ferroelectric effect, the Li/10%BTO/Li cell demonstrated the lowest overpotential of just 0.069 V and 0.265 V after 400 cycles of 0.2 mA cm^{-2} and 0.5 mA cm^{-2}, respectively. In addition, Li/10%BTO/Li also exhibited better cycle stability when compared to other samples (i.e., just 50 cycles for 0%BTO, 200 cycles for 2%BTO, and 260 cycles for 5%BTO at 0.5 mA cm^{-2}).

The morphologies of Li deposits were characterized after 40 cycles and 100 cycles of 0.5 mA cm^{-2}, as shown in Figure 4c. Compared with the irregularly deposited particles for 0%BTO, the addition of BTO does improve the regularity of Li deposits. Even after 100 cycles of 0.5 mA cm^{-2}, the large area of regular Li deposition with uniform size (see SI, Figure S14) is maintained on the surface of the electrolyte for the Li/10%BTO/Li cells, indicating the surface structural stability during the long-term lithiation/delithiation process. In addition, many numerous holes and irregular decomposition products present in Li/0%BTO/Li and Li/2%BTO/Li cells, as displayed in SI, Figure S15, further reveal the severe dendrite growth and interface degradation in the ASSLBs without BTO or with fractional BTO. In contrast, 5%BTO and 10%BTO present smooth surface morphology and even the presence of BTO nanofibers. Additionally, the symmetry plating/stripping curves and the regular morphologies formed which are consistent with that of one side deposition, also confirm the positive effect of the piezo/ferroelectric field in the delithiation process. The

depolarization electric field of BTO reduces the localized excessive concentration of Li$^+$, optimizes the heterogeneity of deposition dynamics, and thus realizes the overall orderly lithiation/delithiation.

To further determine the components of the Li surface after different cycles, XPS measurement was adopted and the detail element content ratios were summarized in Figure 4d. It can be seen that the Li, N, S, F of 0%BTO show a sharp decline, and are replaced by rich C elements during the cycle. With increasing BTO content, the element ratio change trend shows a little which infers to the stable SEI film.[42, 43] And the highest Li element ratio of 22% reflects the thinner SEI film formed on the Li surface for 10%BTO. Moreover, the detected richer and steadier RO-Li, Li$_3$N, Li$_2$O, and Li$_2$S on the Li surface of the rich-BTO electrolyte, as displayed in SI, Figures S16a-c, indicates the formation of Li-containing SEI film with excellent electrochemical stability and well Li$^+$ conduction.[44] The ratio of F and LiF contents was found to increase with increasing cycle number (SI, Figure S16d), further indicating the better evolution of SEI film for the rich-BTO electrolyte.

The ASSLBs using LiFePO$_4$ cathode were assembled to further demonstrate the potential of BTO-based electrolytes. As shown in **Figure 5**a, the BTO addition does not change the initial Coulombic efficiency (ICE) but slightly increased the polarization potential. The electrochemical performance, in this case, was found to mostly depend on the kinetic limitation of cathode and electrolyte, which differs from that of Li/solid electrolyte/Li cells.[15] Therefore, LFP/10%-BTO/Li does exhibit inferior specific capacity at high current density (> 1 C, 1 C=170 mAh g^{-1}), as shown in Figure 5b, demonstrating the lower conductivity for BTO-based electrolytes, which can be explained by the low conductivity desired in ferroelectric materials that is essential for the polarization effects. In contrast, the cycling performance has been significantly improved with increasing BTO content possibly due to superior structural stability of the host material (see Figures 5c-d). Compared to the

LFP/0%BTO/Li cells whose capacity rapidly decays after 100 cycles, the LFP/10%BTO/Li cells still maintain a high discharge capacity of 136.1 Ah g^{-1} and a capacity retention ratio of 91.8% after 300 cycles at 0.5 C. Moreover, as the current density rises to 1 C, the LFP/0%BTO/Li cell just remained stable for 30 cycles, but the LFP/10%BTO/Li cell showed a stable ultralong cycling life with a reversible capacity of 103.2 mAh g^{-1} and a capacity retention ratio of 78.8% after 500 cycles at 1 C. In addition, it also exhibits an ultrahigh average Coulombic efficiency of 99.8% from the 3rd cycle to the 500th cycle.
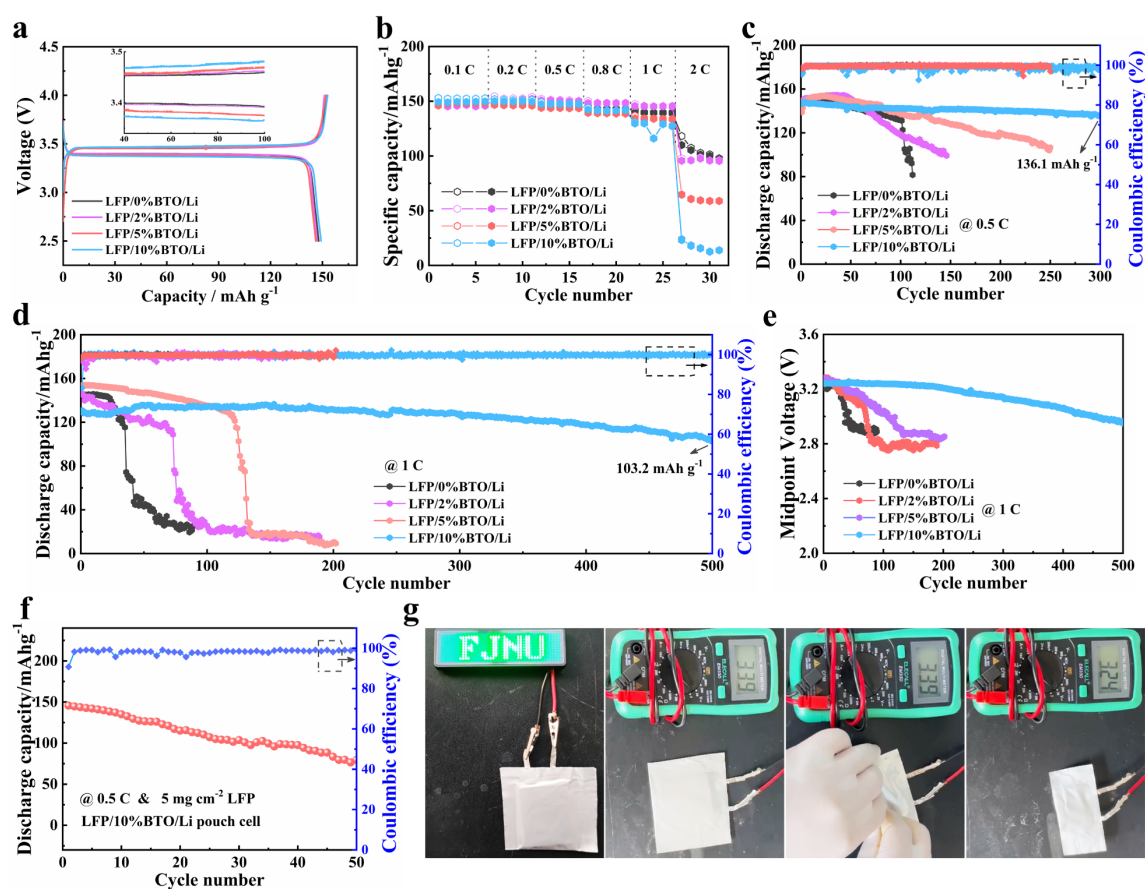

Figure 5. (a) The initial discharge/charge curves of all LFP/solid electrolyte/Li batteries at 0.1 C, (b) Rate performance of all LFP/solid electrolyte/Li batteries, (c) Cycling performance at 0.5 C with two 0.1 C cycles at 60 ℃. (d) Cycling performance at 1 C with two 0.1 C cycles and (e) the corresponding midpoint voltage-cycle number curves at 60 ℃. (f) Cycling performance of LFP/10%BTO/Li pouch cells at 0.5 C at 60 ℃. (g)The destructive condition test of LFP/10%BTO/Li pouch cells is folded and cut into pieces state.

As shown in Figure S17 and Figure 5e, the charge-discharge curves of different cycles

and the midpoint voltage curves further prove that BTO mainly achieves circulation improvement via improving interfacial stability and remaining low polarization due to the ameliorative lithiation/delithiation process. To further appraise the practical application of BTO-based electrolytes, the LFP/10%BTO/Li pouch cells as prepared by 5 mg cm^{-2} LFP and 100 μm Li metal are assumed and measured at 0.5 C at 60 °C. As shown in Figure 5f, the pouch cell delivers a reversible capacity of 80.0 mAh g^{-1} over 50 cycles. Figure 5g and SI, Video S5 manifest that the pouch cells can still maintain a stable open-circuit voltage even after bending or cutting into pieces. Remarkably, it can also light up a green LED (FJNU pattern) with a strong glow easily, indicating the safety and reliability of such solid electrolytes for ASSLBs.

The inferior electrochemical performance for BTO-rich electrolytes indicates the limitation of the fraction of the piezo/ferroelectric phase since the low conductivity of BTO is orthogonal to the expected superionic behavior in solid-state electrolytes. Nevertheless, the decrease in conductivity due to the addition of BTO is offset by reduced Li dendrite formation. Inspired by the fact that the piezo/ferroelectric effect mainly occurs at the shallow Li/electrolyte interface, we firstly add 10%BTO as a modified layer on the 0%BTO to obtain a 0%BTO-10%BTO composite electrolyte (see **Figure 6**a). As shown in Figure 6b, the LFP/0%BTO-10%BTO/Li cell presents a similar average discharge specific capacity of 102.0 mAh g^{-1} at 2 C than that of LFP/0%BTO/Li. The discharge curves at 2 C (SI, Figure S18) manifest that the LFP/0%BTO-10%BTO/Li cells have a higher and more stable discharge platform, suggesting the positive effect of 10%BTO. Moreover, as shown in Figure 6c, the LFP/0%BTO-10%BTO/Li cells deliver better cycling performance with a high discharge capacity of 128.0 Ah g^{-1} and a capacity retention ratio of 88.6% after 200 cycles of 1 C than the poor one of LFP/0%BTO/Li.

A single polymer electrolyte does not represent all the solid electrolytes. To verify the

universality of this strategy, as illustrated in Figure 5d, we further directly compound BTO nanofibers with Li_6PS_5Cl (LPSC) powder to prepare the composite inorganic electrolyte and the corresponding ASSLBs. As shown in Figure 6e, the critical current density (CCD) of the Li/LPSC/Li cell is only 0.45 mA cm^{-2} at 25 °C before adding BTO. In contrast, Li/LPSC-BTO/LPSC/LPSC-BTO/Li still maintains a stable charge-discharge process during the cycle with a cumulative current density step of 0.05 mA cm^{-2} and exhibits a normal non-jumping voltage curve at the current density up to 1 mA cm^{-2}. The successful improvement in CCD indicates that the piezo/ferroelectric effect of BTO is also valid for the sulfide electrolytes. In addition, as shown in SI, Figure S19, the charge-discharge curves show that the addition of BTO can improve ICE and reduce polarization of the full cell. As excepted, the LCO/LPSC/LPSC-BTO/Li-In cell presents much better electrochemical stability, which delivers a high discharge capacity of 86.4 mAh g^{-1} with and a capacity retention ratio of 86.6% at 0.4 C over 200 cycles (see SI, Figure 6g).
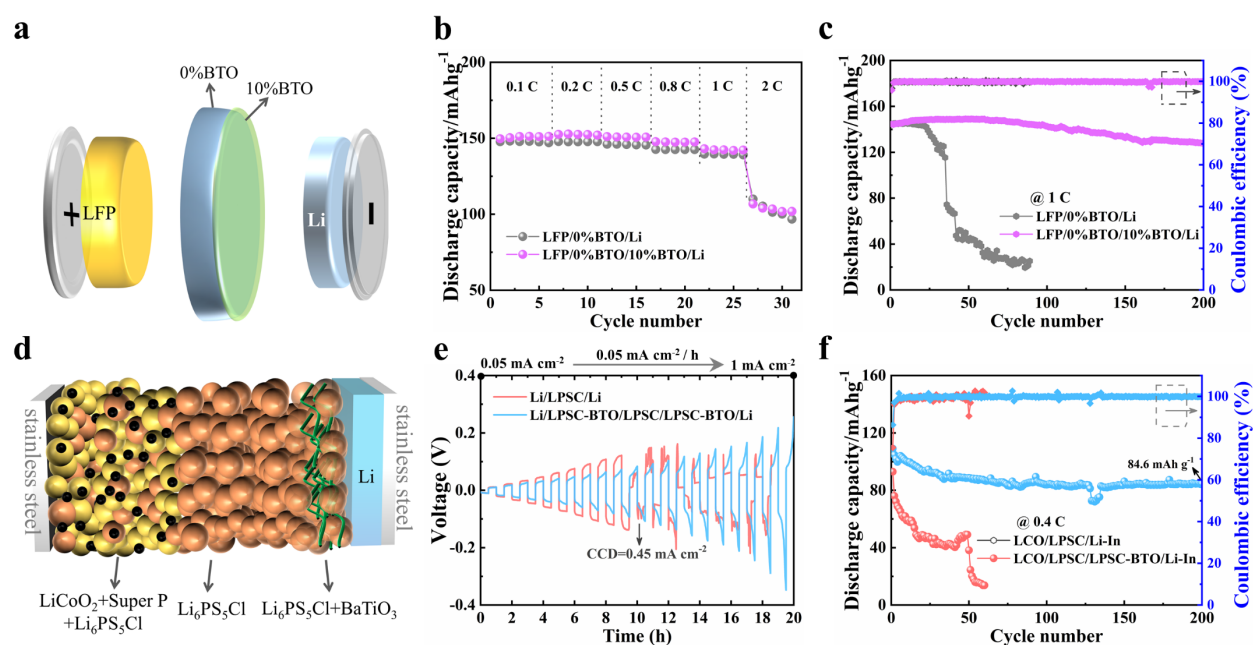

Figure 6. (a) The design diagram for 0%BTO-10%BTO composite solid electrolyte and the battery schematic diagram. (b) Rate performance and (c) Cycling performance at 1 C with two 0.1 C cycles at 60 °C for the LFP/0%BTO/Li and LFP/0%BTO-10%BTO/Li cells. (d) The sulfide solid-state battery schematic diagram. (e) Representative potential response of the Li/LPSC/Li and

Li/LPSC-BTO/LPSC/LPSC-BTO/Li cells undergoing a CCD measurement at 25 °C. (f) Cycling performance at 0.4 C at 25 °C for the LCO/LPSC/Li-In and LCO/LPSC/LPSC-BTO/Li-In cells.

3. Conclusions

We have proposed a concept of multifunctional solid electrolytes based on solid-state lithium electrolytes incorporating small amounts of piezo/ferroelectric phases. The results obtained confirmed a positive role of polarization fields in regulating Li deposition verified by both simulation and experimental data. Theoretical simulation revealed that the piezoelectric field generated under operating condition can actively combat the driving force responsible for dendrite formation at high curvature electrode-electrolyte interface. In addition, the in-built ferroelectric field also decreases the overpotential directly, thus optimizing the Li^+ flux distribution and facilitating an orderly Li deposition. For the validation of the proposed hypothesis, solid electrolytes with piezo/ferroelectric effects were synthesized by adding BTO nanofibers into the PEO/Garnet composite solid electrolyte. The corresponding PFM, in-situ EIS, and SEM results further confirmed their positive role, as predicted by theoretical studies, which helped reduce local overpotential and regulate Li^+ and electron flow. As a result, the LiFePO$_4$/Li batteries using electrode material with 10% BTO showed an ultralong cycle life with a reversible capacity of 103.2 mAh g^{-1} and an ultrahigh average Coulombic efficiency of 99.8% over 500 cycles at 1 C. The corresponding pouch cells exhibited comparable cyclability and allowed bending and even cutting of the pouches. Moreover, the proposed strategy was verified and adopted in the Li$_6$PS$_5$Cl electrolyte to improve the critical current density and cycling performance, demonstrating its universal and promising application. The results presented here demonstrate the role of multi-modal materials in counterbalancing the functional performance in all solid-state LIBs. Despite their intrinsically low electrical conductivity, BTO fibers were beneficial in improving the safety and cycling characteristics by creating internal fields that reduced the Li deposition

and segregation behavior and improving the mechanical stability of the composite material due to the reinforcement of 1D BTO fillers that can deflect mechanical degradation such as crack propagation processes. The proposed strategy provides new opportunities to achieve dendrite-free cycling that is highly relevant for ASSLBs, and relates electrochemical fields.

Acknowledgments

References

[1]   Q. Zhao, S. Stalin, C.-Z. Zhao, L. A. Archer, *Nat. Rev. Mater.* **2020**, *5*, 229.

[2]   C. P. Grey, D. S. Hall, *Nat. Commun.* **2020**, *11*, 6279.

[3]   Z. Hong, V. Viswanathan, *ACS Energy Lett.* **2018**, *3*, 1737.

[4]   Z. Zhang, J. Zhang, H. Jia, L. Peng, T. An, J. Xie, *J. Power Sources* **2020**, *450*, 227601.

[5]   T. Shi, Q. Tu, Y. Tian, Y. Xiao, L. J. Miara, O. Kononova, G. Ceder, *Adv. Energy Mater.* **2020**, *10*, 1902881.

[6]   M. Sakuma, K. Suzuki, M. Hirayama, R. Kanno, *Solid State Ionics* **2016**, *285*, 101.

[7]   K. Shi, Z. Wan, L. Yang, Y. Zhang, Y. Huang, S. Su, H. Xia, K. Jiang, L. Shen, Y. Hu, S. Zhang, J. Yu, F. Ren, Y.-B. He, F. Kang, *Angew. Chemie Int. Ed.* **2020**, *59*, 11784.

[8]   T. Deng, L. Cao, X. He, A.-M. Li, D. Li, J. Xu, S. Liu, P. Bai, T. Jin, L. Ma, M. A.

Schroeder, X. Fan, C. Wang, *Chem* **2021**, *7*, 3052.

[9]   F. Zheng, M. Kotobuki, S. Song, M. O. Lai, L. Lu, *J. Power Sources* **2018**, *389*, 198.

[10] J. Schmidt, M. R. G. Marques, S. Botti, M. A. L. Marques, *npj Comput. Mater.* **2019**, *5*, 83.

[11] L. Chen, H. W. Zhang, L. Y. Liang, Z. Liu, Y. Qi, P. Lu, J. Chen, L. Q. Chen, *J. Power Sources* **2015**, *300*, 376.

[12] P. Barai, K. Higa, V. Srinivasan, *Phys. Chem. Chem. Phys.* **2017**, *19*, 20493.

[13] D. H. Liu, Z. Bai, M. Li, A. Yu, D. Luo, W. Liu, L. Yang, J. Lu, K. Amine, Z. Chen, *Chem. Soc. Rev.* **2020**, *49*, 5407.

[14] H. Liu, X. B. Cheng, J. Q. Huang, H. Yuan, Y. Lu, C. Yan, G. L. Zhu, R. Xu, C. Z. Zhao, L. P. Hou, C. He, S. Kaskel, Q. Zhang, *ACS Energy Lett.* **2020**, *5*, 833.

[15] Z. Yu, X. Zhang, C. Fu, H. Wang, M. Chen, G. Yin, H. Huo, J. Wang, *Adv. Energy Mater.* **2021**, *11*, 2003250.

[16] D. Cao, X. Sun, Q. Li, A. Natan, P. Xiang, H. Zhu, *Matter* **2020**, *3*, 57.

[17] X. Guo, Y. Ding, G. Yu, *Adv. Mater.* **2021**, *33*, 2100052.

[18] T. Ogunfunmi, N. Ebechidi, R. Ahmed, O. Oyewole, J. Obayemi, W. Soboyejo, *MRS Adv.* **2021**, *6*, 154.

[19] S. Luo, Z. Wang, X. Li, X. Liu, H. Wang, W. Ma, L. Zhang, L. Zhu, X. Zhang, *Nat. Commun.* **2021**, *12*, DOI 10.1038/s41467-021-27311-7.

[20] Z. Li, J. Huang, B. Yann Liaw, V. Metzler, J. Zhang, *J. Power Sources* **2014**, *254*, 168.

[21] J. Zhu, X. L. Li, C. Wu, J. Gao, H. Xu, Y. Li, X. Guo, H. Li, W. Zhou, *Angew. Chemie - Int. Ed.* **2021**, *60*, 3781.

[22] C. Kim, J. Kim, J. Park, J. Kim, S. Lee, S. Sun, S. Myung, D. Lee, K. Park, I. Jang, S. Kim, H. Lee, H. Jung, U. Paik, T. Song, *Adv. Energy Mater.* **2021**, *11*, 2102045.

[23] S. Liu, Y. Zhao, X. Li, J. Yu, J. Yan, B. Ding, *Adv. Mater.* **2021**, *33*, 2008084.

[24] C. Wang, M. Liu, M. Thijs, F. G. B. Ooms, S. Ganapathy, M. Wagemaker, *Nat. Commun.* **2021**, *12*, 6536.

[25] B.-F. Cui, X.-P. Han, W.-B. Hu, *Small Struct.* **2021**, *2*, 2000128.

[26] D. Rehnlund, C. Ihrfors, J. Maibach, L. Nyholm, *Mater. Today* **2018**, *21*, 1010.

[27] M. H. Braga, *Mater.* **2021**, *14*, DOI 10.3390/ma14092398.

[28] K. Singh, S. Rokade, *J. Power Sources* **1984**, *13*, 151.

[29] E. A. Il'ina, A. A. Raskovalov, B. D. Antonov, V. B. Malkov, *Russ. J. Appl. Chem.* **2015**, *88*, 775.

[30] O. Kolosov, A. Gruverman, J. Hatano, K. Takahashi, H. Tokumoto, *Phys. Rev. Lett.* **1995**, *74*, 4309.

[31] M. Rivas, V. Vyas, A. Carter, J. Veronick, Y. Khan, O. V Kolosov, R. G. Polcawich, B. D. Huey, *J. Mater. Res.* **2015**, *30*, 429.

[32] M. Budimir, D. Damjanovic, N. Setter, *J. Appl. Phys.* **2003**, *94*, 6753.

[33] J. Hlinka, P. Ondrejkovic, P. Marton, *Nanotechnology* **2009**, *20*, 105709.

[34] A. Ichangi, V. V Shvartsman, D. C. Lupascu, K. Lê, M. Grosch, A. Kathrin Schmidt-Verma, C. Bohr, A. Verma, T. Fischer, S. Mathur, *J. Eur. Ceram. Soc.* **2021**, *41*, 7662.

[35] J. Xiang, Z. Cheng, Y. Zhao, B. Zhang, L. Yuan, Y. Shen, Z. Guo, Y. Zhang, J. Jiang, Y. Huang, *Adv. Sci.* **2019**, *6*, 1901120.

[36] H. Tu, S. Wang, H. Jiang, Z. Liang, D. Shi, Y. Shao, J. Shen, Y. Wu, X. Hao, *J. Mater. Chem. A* **2020**, *8*, 16661.

[37] R. Gu, K. Yu, L. Wu, R. Ma, H. Sun, L. Jin, Y. Xu, Z. Xu, X. Wei, *Ceram. Int.* **2019**, *45*, 8243.

[38] F. Dinelli, F. Fabbri, S. Forti, C. Coletti, O. V Kolosov, P. Pingue, *Nanomater.* **2020**, *10*, 2494.

[39] Y. Guo, R. Wang, C. Cui, R. Xiong, Y. Wei, T. Zhai, H. Li, *Nano Lett.* **2020**, *20*, 7680.

[40] M. H. Braga, J. E. Oliveira, A. J. Murchison, J. B. Goodenough, *Appl. Phys. Rev.* **2020**, *7*, 11406.

[41] G. Bieker, M. Winter, P. Bieker, *Phys. Chem. Chem. Phys.* **2015**, *17*, 8670.

[42] C. Yan, X.-B. Cheng, Y. Tian, X. Chen, X.-Q. Zhang, W.-J. Li, J.-Q. Huang, Q. Zhang, *Adv. Mater.* **2018**, *30*, 1707629.

[43] S. Qi, H. Wang, J. He, J. Liu, C. Cui, M. Wu, F. Li, Y. Feng, J. Ma, *Sci. Bull.* **2021**, *66*, 685.

[44] H. Xu, P.-H. Chien, J. Shi, Y. Li, N. Wu, Y. Liu, Y.-Y. Hu, J. B. Goodenough, *Proc. Natl. Acad. Sci.* **2019**, *116*, 18815.